Hydrol. Earth Syst. Sci., 30, 7301–7317, 2026
https://doi.org/10.5194/hess-30-7301-2026
© Author(s) 2026. This work is distributed under
the Creative Commons Attribution 4.0 License.

Hydrology and Earth System Sciences
Open Access
EGU

Summer land-atmosphere coupling over Europe: a comparative evaluation of observation-based datasets

Monalisa Sahoo[1], **Stefano Materia**[1,2], **and Markus G. Donat**[1,3]

[1]Barcelona Supercomputing Center, Barcelona, Spain
[2]CMCC Foundation – Euro-Mediterranean Center on Climate Change, Bologna, Italy
[3]Institució Catalana de Recerca i Estudis Avançats (ICREA), Barcelona, Spain

Correspondence: Monalisa Sahoo (monalisa.sahoo@bsc.es)

Received: 3 June 2026 – Discussion started: 30 June 2026
Revised: 28 October 2026 – Accepted: 5 November 2026 – Published: 26 November 2026

Abstract. Land–atmosphere coupling has long been recognized to modulate the surface fluxes partitioning in transitional evaporative regimes, where soil moisture anomalies control evapotranspiration. However, globally available in situ observations for these variables remain limited. This study provides a comprehensive assessment of the similarities, dissimilarities, and limitations among gridded observations-based datasets of surface soil moisture, evapotranspiration, potential evapotranspiration, and 2 m air temperature across Europe. The analysis focuses on the IPCC-defined regions of Northern Europe, Eastern Europe, Western-Central Europe, and the Mediterranean during summer (June–August) for the recent 20-year period (2003–2022), and evaluates and compares the representation of land–atmosphere coupling across the different datasets. Results show that while there are relevant differences across datasets in their absolute values and seasonal variations, the interannual variation of the state variables and the spatial variability of land-atmosphere coupling are mostly consistent across the different datasets. The surface soil moisture is the most consistent, showing significant correlations across all datasets, whereas evapotranspiration shows large inconsistency among datasets for Western-Central Europe and the Mediterranean. Some reanalysis datasets exhibit unrealistic annual cycle patterns across variables and regions, which is also reflected in their coupling representation in both temporal and spatial structures.

1 Introduction

Soil moisture and radiation regulate the surface fluxes through the exchange of water and energy between the soil and air. Being part of the land water and energy balance equations, evapotranspiration allows for the development and sustenance of land-atmosphere coupling processes. The coupling between land surface and atmosphere is an important modulator of climate as it influences the long-term environmental changes by affecting the precipitation, surface fluxes, evapotranspiration, and temperature (Seneviratne et al., 2010).

Two key pathways can be identified in the land-atmosphere coupling mechanism (Dirmeyer, 2006; Ferguson et al., 2012). The land pathway is the interaction between soil moisture and surface fluxes, that becomes critical in transitional evaporative regimes where soil moisture limitation can heavily constrain evapotranspiration. The atmospheric pathway is the response of air temperature to changes in evapotranspiration. Therefore, a two-legged land-atmosphere coupling is characterized by the interaction between soil moisture and air temperature (Dirmeyer et al., 2014). In transitional evaporative regimes, these variables are negatively correlated: reductions in soil moisture lead to higher air temperatures, which in turn promote further soil drying (Fischer et al., 2007; Vautard et al., 2007; Hirschi et al., 2011; Santanello et al., 2011; Hirsch et al., 2014; Donat et al., 2017; Philip et al., 2018; Dirmeyer et al., 2021). Scarce precipitation in preceding seasons can trigger this feedback loop and amplify hot summer temperature extremes (Miralles et al., 2019; Byrne, 2021; Mukherjee et al., 2023). A few studies have shown that Coupled Model Intercomparison Project

Phase 5 (CMIP5) models which represent stronger land–atmosphere coupling in the present climate have a tendency to project larger increase in frequencies of future hot extremes (Donat et al., 2018). Moreover, the separation between latent and sensible heat fluxes influences the intensity and duration of extreme heat waves and droughts (Materia et al., 2022; Knist et al., 2017). When soils contain sufficient moisture, evaporation cools the boundary layer by removing heat from the surface. In contrast, dry soils reduce evaporation, causing more energy to convert into sensible heat, which warms the air and intensifies extreme hot events. Hence, soil moisture–temperature coupling is critical in transitional evaporative regimes, where soil water scarcity limits evapotranspiration, particularly during summer, creating the ground for more intense, longer-lasting heatwaves (Koster et al., 2006; Seneviratne et al., 2006; Lorenz et al., 2010; Miralles et al., 2014; Dirmeyer and Halder, 2017).

Besides, vegetation also acts as a critical dynamic mediator in land-atmosphere coupling processes. By modulating stomatal conductance in response to fluctuating soil water availability and shifting atmospheric demand, vegetation strongly regulates the feedback loop between soil moisture and evapotranspiration (Denissen et al., 2022). Consequently, transpiration rates vary sharply across climates, remaining markedly higher in energy-limited regions compared to water-stressed arid and semi-arid ecosystems (Li et al., 2022a, 2021). This physiological regulation introduces a distinct nonlinearity into the relationship between soil moisture and surface evaporation (Williams and Torn, 2015; Schlesinger and Jasechko, 2014). Furthermore, structural canopy characteristics, such as vegetation type and the leaf area index (LAI), exert a profound control on both plant transpiration and direct soil evaporation (Baldocchi and Meyers, 1998). While a higher LAI generally expands the total transpirational surface area, densely closed canopies simultaneously suppress direct soil evaporation by intercepting solar radiation, and can concurrently moderate transpiration through internal canopy self-shading.

Given the complexity of land-atmosphere coupling and the likely expansion of transitional regimes in the future (Seo and Ha, 2022), it is important to enhance our understanding by exploring the coupling further, while global observational capabilities remain limited and climate models still struggle to accurately represent these processes (Miralles et al., 2019; Quesada et al., 2012).

Observations of soil moisture are primarily obtained through in situ measurements and microwave remote-sensing satellites. The in situ stations provide accurate point-scale observations, however, their spatial coverage is extremely limited and uneven (Nguyen et al., 2017; Li et al., 2020; Wu et al., 2021). Satellite retrievals provide broader spatial coverage but are generally limited to the surface layer soil moisture and might have significant uncertainties due to complex land surface conditions, limitations due to the presence of dense cloud cover, and retrieval algorithms (Kim et al., 2018; Mousa and Shu, 2020; Zhuo et al., 2015). To fill these observational gaps, reanalysis products and land surface models have become essential tools for providing continuous spatially gridded global soil moisture data (Li et al., 2020).

Despite the advancements, reliability of reanalysis and model-based soil moisture still remain a main concern in the context of climate change impact studies (Thorne and Vose, 2010). Given its importance in modulating the intensity and duration of hot extremes in many regions of the world (Donat et al., 2017), robust soil moisture datasets are urgently needed to assess environmental impacts and guide adaptation strategies under a changing climate.

Evapotranspiration also remains poorly measured at the global scale because it cannot be directly observed over large spatial domains and must instead be inferred from indirect measurements, remote sensing products, or model simulations, each of which introduces substantial uncertainty (Tran et al., 2023; Yi et al., 2024). Evapotranspiration plays a crucial role in completing the energy/water cycles (Xu et al., 2024). A large amount of incoming solar radiation is used for evapotranspiration in the form of latent heat, regulating the surface energy budget (Trenberth et al., 2009). The evapotranspiration rate primarily depends on water and energy availability. Potential evapotranspiration (PET) represents the maximum possible water loss to the atmosphere, including water loss from evaporation and plant transpiration – under conditions of unlimited water supply (Thornthwaite, 1948), and depends on temperature, wind, and humidity (Allen et al., 1998). Changes in PET and precipitation modulate the amount of water in the soil. An increase in atmospheric demand for water indicates that PET and evapotranspiration increase. These changes can be very rapid and affect the transition of a water-limited region to an arid-type climate, even if changes in precipitation occur at a slower pace (Cook et al., 2014; Sherwood and Fu, 2014; Xu et al., 2024). Therefore, accurate representation of evapotranspiration and PET is essential for understanding the hydrological cycle and land-atmosphere interaction changes, and for supporting water resource management and drought forecasting (Dembélé et al., 2020).

With the availability of the vast number of data sources for observations and advancements in data processing methods, further evaluation is essential to guide the effective and efficient use of diverse soil moisture and evapotranspiration datasets. Therefore, the overarching objective of this study is to assess similarities and uncertainties among various observations-based datasets, particularly for variables related to land–atmosphere coupling – namely soil moisture, evapotranspiration, potential evapotranspiration, and 2 m mean air temperature. In addition, this study examines how different datasets represent the individual land and atmospheric coupling pathways, as well as their overall land-atmosphere coupling. Here we comprehensively compare various observational data sources, including satellite products (ESA-CCI), satellite-derived estimates (GLEAM versions), reanal-



Figure 1. Study area: IPCC reference regions (Iturbide et al., 2020).

ysis datasets, and gridded in situ observations, focusing on Europe. Although vegetation plays a crucial role in land-atmospheric coupling, it is not explicitly explored in this study.

2 Data and methodology

2.1 Data

For this observations-based data comparison, all the data are taken for a common period of the recent 20 years (2003–2022, except FLUXCOM and SiTHv2 for which data are only available till 2020) over European IPCC regions (i.e., Northern Europe (NEU), Western Central Europe (WCE), Eastern Europe (EEU), and Mediterranean (MED); Fig. 1; Iturbide et al., 2020). The datasets details are described in the following subsections, and more details regarding the variables, temporal frequency, etc, used in this study are listed in Table 1.

2.1.1 Global land evaporation Amsterdam Model (GLEAM)

The Global Land Evaporation Amsterdam Model (GLEAM) is a satellite remote sensing-based model designed for the estimation of evaporation and soil moisture globally (Miralles et al., 2011). The version of GLEAM (version 3) used in this study, is available in daily frequency with a spatial resolution of 0.25° (Martens et al., 2017). All the components are estimated at each grid using a Priestley and Taylor-based (Priestley and Taylor, 1972) formulation for potential evapotranspiration. GLEAM 3.8a spans a period from 1980 to near-present and is driven by a combination of satellite- and reanalysis-based forcings, whereas GLEAM 3.7b spans from 2003 to the present and is driven entirely by satellite-based forcing data.

2.1.2 ECMWF reanalysis v5 (ERA5)

ERA5 is the fifth generation of the ECMWF reanalysis based on the Integrated Forecasting System (IFS) version CY41R2. Measurements from various observations systems are assimilated into the atmospheric model using a 4D-Var scheme (Hersbach et al., 2020). ERA5 provides 137 hybrid sigma/-pressure levels of the atmosphere from the surface up to 1 Pa. The grid resolution is 31 km. Data are provided at a hourly frequency and provide global spatial coverage from 1940 until the present.

ERA5land is produced by rerunning the land component from ERA5 atmospheric reanalysis with a higher spatial resolution of 0.1°. The model used for ERA5land is the tiled ECMWF Scheme for Surface Exchanges over Land incorporating land surface hydrology (H-TESSEL) (Muñoz-Sabater et al., 2021), forced by the ERA5's atmospheric fields. Data are provided from 1950 to the present at an hourly frequency over land regions only.

2.1.3 European Space Agency Climate Change Initiative (ESA CCI) soil moisture

The ESA CCI soil moisture dataset is provided by the Climate Change Initiative program of the European Space Agency. ESA CCI, as a satellite product, only provides the surface layer soil moisture and is primarily composed of three types of daily frequency dataset sources, i.e., active, passive, and active-passive combined microwave products (Dorigo et al., 2017; Gruber et al., 2019; Preimesberger et al., 2020). Here, we select the daily combined microwave products of version 8.1 with a spatial resolution of 0.25°. The data is available from 1991 until recent time.

2.1.4 E-OBS

The E-OBS dataset (Cornes et al., 2018) provides daily gridded surface variables at 0.1 and 0.25° resolution over Europe covering the area 25° N–71.5° N, 25° W–45° E. The dataset is prepared by collection from station data collated by the ECA&D (European Climate Assessment & Dataset) initiative (Klein et al., 2002). In the present study, we use the dataset's version 29 at 0.25° resolution for mean, maximum, and minimum temperatures at 2 m.

2.1.5 FLUXCOM

FLUXCOM uses machine learning to merge energy flux measurements from FLUXNET eddy covariance towers with remote sensing and meteorological data to estimate global gridded net radiation, latent heat flux, sensible heat flux, and their uncertainties (Jung et al., 2019). The FLUXCOM provides data in two resolutions: high resolution of 0.0833° using MODIS remote sensing data, and low resolution of 0.5° using remote sensing and meteorological data. It uses seasonal vegetation variables and indices from either measured

Table 1. Observations-based datasets used in this study, data type, resolution, temporal frequency, analysis period, and variables. Variables in bold indicate fields that are derived from other provided variables.

Data	Data type	Res.	Freq.	Years	Variables
ESA-CCI	Satellite	0.25°	Daily	2003–2022	Surface soil moisture
FLUXCOM	In situ	0.5°	Daily	2003–2020	Latent heat flux, **Evapotranspiration**
E-OBS	Gridded In situ	0.25°	Daily	2003–2022	Surface air temperature, Maximum air temperature, Minimum air temperature, **Potential evapotranspiration**
GLEAM	land evaporation Model	0.25°	Daily	2003–2022	Surface soil moisture, Evapotranspiration, Potential evapotranspiration
SiTHv2	eco-hydrological Model	0.1°	Daily	2003–2020	Surface soil moisture, Evapotranspiration
ERA5/ ERA5land	Reanalysis	0.25°/0.1°	Daily	2003–2022	Surface soil moisture, Latent heat flux, Net surface longwave radiation, Net surface shortwave radiation, **Evapotranspiration**, Surface air temperature, Maximum air temperature, Minimum air temperature, **Potential evapotranspiration**
MERRA2	Reanalysis	0.5° × 0.625°	Daily	2003–2022	Surface soil moisture, Evapotranspiration, Surface air temperature, Maximum air temperature, Minimum air temperature, **Potential evapotranspiration**
JRA55	Reanalysis	1.25°	Daily	2003–2022	Surface soil moisture, Evapotranspiration, Surface air temperature, Maximum air temperature, Minimum air temperature, **Potential evapotranspiration**

at the flux tower sites or retrieved from the ERA-Interim (Dee et al., 2011). In this study, we use a 0.5° resolution latent heat flux to calculate evapotranspiration.

2.1.6 Simple Terrestrial Hydrosphere model, version 2 (SiTHv2)

The Terrestrial Hydrosphere model, version 2 (SiTHv2) is an eco-hydrological model. It is driven by multi-source satellite observations and hydrometeorological variables from reanalysis data. It provides daily global evapotranspiration and soil moisture at a 0.1° spatial resolution (Zhang et al., 2024). The global soil type used in this model is acquired from the Harmonized World Soil Database version 1.2 (Wieder et al., 2014). For vegetation dynamics, the leaf area index from the European Geoland2/BioPar project Version 2 is used (Baret et al., 2013). Annual land cover dynamics are taken from the Historic Land Dynamics Assessment+ product (Winkler et al., 2021). The Global Land Surface Satellite product (Liang et al., 2021) is used for surface albedo and emissivity observations. Daily air temperature and air pressure data are taken from the Multi-Source Weather product (Beck et al., 2022), and radiation and precipitation data from ERA5 (Muñoz-Sabater et al., 2021).

2.1.7 Japanese 55-year reanalysis (JRA-55)

The Japan Meteorological Agency (JRA55) reanalysis provides land analyses by running an offline land model with forcing from an atmospheric model (Kobayashi et al., 2015). The data are available in a 320×640 Gaussian grid from 1958 to 2024. We have taken surface soil moisture, evapotranspiration, surface air temperature, maximum air temperature, and minimum air temperature from JRA55 in this study.

2.1.8 Modern-Era Retrospective analysis for Research and Applications version 2 (MERRA2)

Modern-Era Retrospective analysis for Research and Applications version 2 (MERRA2) is a global atmospheric reanalysis produced by NASA's Global modeling and Assimilation office (Gelaro et al., 2017). It has 0.5° (latitude) ×0.625° (longitude) spatial resolution, with vertical 72 hybrid sigma-pressure layers from the surface to 0.01 hPa at hourly frequency. We have used surface soil moisture, evapotranspiration, surface air temperature, maximum air temperature, and minimum air temperature in this study.

2.2 Methodology

To study the coupling metrics of land and atmosphere in the best possible way, the ERA5land and SiThv2 data variables are re-gridded to the resolution of the ERA5 data. Similarly, the ESA-CCI and E-OBS data are re-gridded to the FLUXCOM resolution. As each of these datasets provides one variable for this land-atmospheric coupling study, unlike the other reanalysis datasets, we use these dataset combinations to represent the different couplings (i.e., land coupling, atmospheric coupling, and land-atmospheric coupling). For this analysis, these three datasets are considered over the common period from 2003 to 2020. Similarly, both the GLEAM versions and SiTHv2 are similar to the reanalysis data type (in Table 1), i.e., land models driven by atmospheric boundary conditions, and do not provide surface air temperature as a variable; we use ERA5 surface air temperature data in combination with GLEAM (both versions) and SiTHv2 for this coupling study. Here, we use Pearson's correlation coefficient (R) and linear regression for this analysis.

In the JRA55 surface soil moisture data, the first day of each month shows abnormally low values. This bias is shown in Fig. 2, but these values are excluded and converted to NaN values in all the successive analyses. Similarly, in both the GLEAM versions (i.e., 3.7b and 3.8a), the evapotranspiration and potential evapotranspiration show abnormally low values for 6 and 7 June each year in some regions (Fig. 2), and are also converted to NaN values. The surface soil moisture from ESA-CCI is only taken from May to November: in fact, a large fraction of missing data is present over most European regions from December to April, mainly due to frozen soils and snow cover, which greatly limit the accuracy of the microwave measurements (Zheng et al., 2023; Preimesberger et al., 2020, 2025) (figures not shown).

For the datasets lacking evapotranspiration and potential evapotranspiration, these variables have been calculated as in Allen et al. (1998):

$$\text{Evapotranspiration} = \frac{\text{LHF}}{2.501 - (2.361 \times 10^{-3}) \times T} \quad (1)$$

This equation takes the density of water equal to $1000\,\text{kg}\,\text{m}^{-3}$. Latent heat flux (LHF) and corresponding temperature (T) from observations or reanalysis are in units of $\text{MJ}\,\text{m}^{-2}\,\text{s}^{-1}$ and °C, respectively, which gives evapotranspiration in units of $\text{kg}\,\text{m}^{-2}\,\text{s}^{-1}$. It is converted to $\text{mm}\,\text{d}^{-1}$ by multiplying the value by 86 400.

PET (Except for GLEAM data, in which PET is provided as a variable to download directly from the data source) is calculated using daily air temperature, maximum temperature, and minimum temperature using the Hargreaves equation (Hargreaves and Samani, 1982), Baier's equation (Baier and Robertson, 1965), and Thornthwaite´s equation (Thornthwaite, 1948) based on the Python package xclim (Logan et al., 2022). Penman-Monteith (Allen et al., 1998) equation based on the Python package PyETo., that uses several atmospheric parameters, is used as well (Note that only the Hargreaves method is shown in the main figures and the others are included in the Supplement for PET analyses only). Equations for each method are as follows:

PET by Hargreaves and Samani (1982):

$$\begin{aligned}\text{PET} &= K \times \text{SR} \times (T + 17.8) \\ &= K \times K_{\text{SR}} \times R_{\text{a}} \times (T + 17.8) \times \sqrt{T_{\max} - T_{\min}}\end{aligned} \quad (2)$$

Where K is a constant, SR is solar radiation in $\text{MJ}\,\text{m}^{-2}\,\text{s}^{-1}$, and T is the daily air temperature in °C units. K_{SR} is a constant, R_{a} is extraterrestrial radiation in $\text{MJ}\,m^{-2}\,\text{s}^{-1}$, and $T_{\max}$ and $T_{\min}$ are the daily maximum and minimum air temperature in °C, respectively.

PET by Baier and Robertson (1965):

$$\begin{aligned}\text{PET} = 0.094 \times (&-87.03 + 0.928 \times T_{\max} \\ &+ 0.933 \times (T_{\max} - T_{\min}) + 0.0486 \times R_{\text{a}}\end{aligned} \quad (3)$$

PET by Thornthwaite (1948):

The xclim Python package calculates PET directly from $T_{\max}$ and $T_{\min}$ through a series of steps. First, it determines the annual Heat Index (I) using the following formula:

$$I = \sum_{i=1}^{12} \left(\frac{T}{5}\right)^{1.514} \quad (4)$$

In the xclim Thornthwaite method, PET is estimated monthly, assuming a 30 d month with 12 theoretical sunshine hours d^{-1}. These values are then adjusted based on the actual month length and theoretical sunshine hours for the specific latitude, using the following equation:

$$\text{PET} = 16 \times \left(\frac{10 \times T}{I}\right)^{\alpha} \times \left(\frac{N}{12} \times d\right) \quad (5)$$

where N is the theoretical sunshine hours for each month, and d is the number of days for each month. α is calculated as:

$$\begin{aligned}\alpha = &675 \times 10^{-9} \times I^3 - 771 \times 10^{-7} \times I^2 + 1792 \\ &\times 10^{-5} \times I + 0.49239\end{aligned} \quad (6)$$

PET by Penmann-Monteith method:

$$\text{PET} = \frac{0.480 \times \Delta \times (R_{\text{n}} - G) + \gamma \times \frac{900}{T+273} \times U_2 \times (e_{\text{s}} - e_{\text{a}})}{\Delta + \gamma \times (1 + 0.34 \times U_2)} \quad (7)$$

where R_{n} is net surface radiation in units of $\text{MJ}\,\text{m}^{-2}\,\text{s}^{-1}$, G is the soil heat flux in $\text{MJ}\,\text{m}^{-2}\,\text{s}^{-1}$, T is 2 m air temperature in °C, U_2 is the wind speed at 2 m height in $\text{m}\,\text{s}^{-1}$, e_{s} and e_{a} are saturation vapor pressure and actual vapor pressure respectively in kPa, Δ is the slope of the saturation vapor pressure curve in $\text{kPa}\,°\text{C}^{-1}$, and γ is the psychometric constant in $\text{kPa}\,°\text{C}^{-1}$.

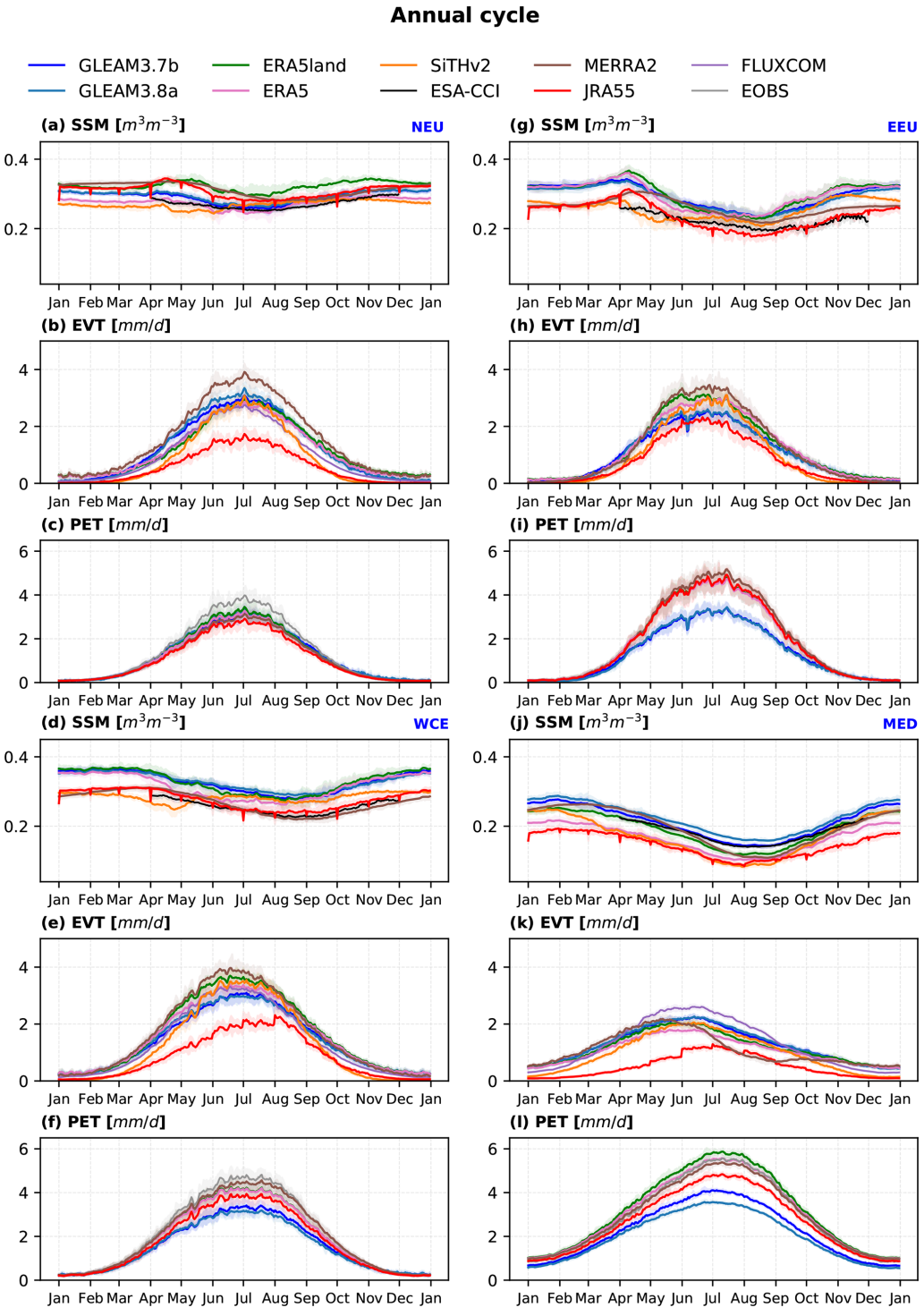


Figure 2. Annual cycle of daily data for SSM (surface soil moisture), EVT (evapotranspiration), and PET (potential evapotranspiration) over four IPCC European regions (NEU: **a**, **b**, **c**; WCE: **d**, **e**, **f**; EEU: **g**, **h**, **i**; MED: **j**, **k**, **l**). The 25th–75th percentile ranges are shown as shaded areas for each data point.

3 Results

3.1 Annual cycle and interannual variation over European regions

To understand the seasonal variation throughout the year, we first analyze the annual cycle at the daily scale for surface soil moisture (SSM), evapotranspiration (EVT), and potential evapotranspiration (PET) across the four IPCC-defined regions: NEU, WCE, EEU, and MED (Iturbide et al., 2020; Fig. 2). JRA55 indicates abnormally low values of SSM on each month's first day, which might be due to model initialization (no such documentation of this error is found in the literature). This issue still might affect their monthly average SSM data, and therefore, the users should be aware of it before using the data in their analysis.

The four regions indicate similar annual cycles for all datasets for each variable, with summer characterized by drier soil moisture, elevated evapotranspiration, and higher PET.

NEU SSM (Fig. 2a) shows low seasonal variability, with SSM decreases during winter and then increases to reach a spring peak, following snow melt. Then summer gets drier, and a secondary wet phase takes place in autumn. As this region experiences wet summers, the seasonal variation of SSM is low, even though the EVT (Fig. 2b) and PET (Fig. 2c) annual cycle indicate a gradual increase during spring and summer. The factual lack of summer water stress also explains the minimal difference between PET and EVT over this region, suggesting that NEU lies in an energy-limited evaporative regime. For the SSM annual cycle (Fig. 2a), SiTHv2 and MERRA2 differ substantially from the rest of the data across all regions. For EVT (Fig. 2b), there is a big difference between MERRA2 and JRA55 (by a factor of $2\,\mathrm{mm\,d^{-1}}$) during summer, while other datasets are much closer to each other and this is also seen for EEU and WCE. For PET (Fig. 2c), E-OBS represents the highest peak and JRA55 the lowest during summer while other datasets are very similar to each other.

Similarly, for EEU, the SSM annual cycle (Fig. 2g) begins with almost stable values in the entire winter, following a steady increase in SSM that peaks in early spring. This is succeeded by a sharp decline at the start of summer, with continued drying through late summer, before SSM rises again to reach a secondary peak in late autumn. The lowest EVT (Fig. 2h) occurs during winter, increasing through spring and peaking in summer, followed by a gradual decline during autumn. Over EEU, GLEAM 3.7b and 3.8a show abnormally low EVT and PET values (Fig. 2i) on 6 and 7 June of each year, therefore, these dates are removed from the GLEAM datasets in the following analysis. The PET annual cycle variation during summer for both GLEAM versions coincide with each other and they are about 2 factors less than for the rest of the datasets. PET variation follows a similar pattern as EVT in both the GLEAM datasets, while summer EVT is considerably lower than summer PET in the other datasets.

SSM variability (Fig. 2d) in the WCE region shows a similar winter with no variability as EEU (Fig. 2g), followed by a gradual decline from spring through summer and mid-autumn, and a renewed increase toward late autumn and early winter. In contrast, EVT (Fig. 2e) and PET (Fig. 2f) are characterized by low values in winter, a steady increase through spring, and a pronounced peak during summer, after which both variables decrease progressively into autumn. This seasonal evolution reflects a coherent annual pattern, with soil moisture mean being highest during the cooler seasons, while evapotranspiration and potential evapotranspiration are at their maximum during the warmest months of the year. During summer, all the datasets shows very distinct peak for PET while all of them are calculated using the same equation (except GLEAM versions) and it is also seen in the case for MED.

The driest soil is found in the MED region (Fig. 2j), especially in the summer, while PET (Fig. 2l) is the highest among all regions. During the summer, there is often not enough soil water available to meet the atmospheric demand, making MED a water-limited region. Therefore, the EVT values are lower during summer compared to other regions despite the higher solar radiation and temperatures. The soil moisture values are similar across datasets, except for JRA55, that shows lower values, and SiTHv2, characterized by a more pronounced seasonal cycle. EVT is also comparable among datasets, apart from an early dip in MERRA2 in mid-summer and a delayed summer peak accompanied by very low values for JRA55. PET follows the temperature annual cycle, with large variability across datasets during the summer.

In the Supplement (Fig. S1), we compare the different PET calculations (only for ERA5land) for all the regions. Baier's method shows a notably narrower range, with PET values remaining at zero during winter and autumn, before abruptly peaking in summer to align with Hargreaves-derived PET values. The Penman-Monteith method applied to ERA5 and ERA5land data shows a slight shift in the timing of the peak relative to the other PET estimates. Hargreaves-based PET also closely matches the GLEAM (3.7b and 3.8a) PET estimates for NEU. Baier's method in MED does not exhibit extended zero values in spring or autumn but instead follows a pattern similar to that of the Hargreaves and Penman-Monteith methods.

There exist substantial differences in the seasonal patterns of PET derived from various estimation methods. These discrepancies are largely attributed to the complexity of the underlying equations and the input variables involved. Generally, the more complex the method, the greater the potential for biases introduced by uncertainties in the input variables. For example, while the Penman-Monteith method is considered physically comprehensive, accounting for temperature, humidity, radiation, and wind speed, it is also more suscep-

tible to compounded errors due to biases in these multiple inputs. Such issues have been well-documented in previous studies (Li et al., 2022b; Trajkovic, 2007; Moratiel et al., 2020).

In contrast, the Hargreaves method offers a simpler and more robust alternative, relying solely on temperature for PET estimation. Given its simplicity and reduced vulnerability to multi-variable bias, we selected the Hargreaves method for PET representation in the following analysis. This choice provides a relatively simple but robust method for intercomparison and interpretation across datasets and regions, without the added uncertainty introduced by more complex formulations. Additionally, applying the Hargreaves method across all datasets is necessary for consistency in this study, as it ensures a uniform approach to PET estimation, which would be more complicated with the Penman-Monteith method due to larger uncertainties across different data sources.

To gain an extensive understanding of the climate dynamics, it is crucial to examine the interannual variability of each variable and the relationships between them, especially in the context of recent trends. This analysis focuses specifically on the summer months–June, July, and August (Fig. 3). Here we only show results for the MED region in the main manuscript and results for the other regions are available in the Supplement (Figs. S2, S3).

The MED region shows low interannual variation in SSM (Fig. 3a) with values ranging from 0.08 to 0.2 $m^3\,m^{-3}$ across all datasets. EVT (Fig. 3c) ranges from around 1 to 2.5 $mm\,d^{-1}$. PET (Fig. 3e) indicates a large range of variations among the datasets,with values ranging from around 3 to 6 $mm\,d^{-1}$. The summers of 2003, 2012, 2017, and 2022 are characterized by low soil moisture and evapotranspiration, following anomalously warm and dry conditions (Wilcox et al., 2018; Kew et al., 2019). Wetter summers like 2004, 2014, and 2018 (Ratna et al., 2017; Beillouin et al., 2020) show local high in SSM and EVT, local low in PET. The SSM correlation matrix (Fig. 3b) indicates significant correlations among datasets. The EVT correlation matrix (Fig. 3d) shows that JRA55 is weakly correlated with ERA5 and FLUXCOM, while SiTHv2 is weakly correlated only with FLUXCOM. The correlation matrix of PET (Fig. 3f) shows that GLEAM 3.7b is weakly correlated with all datasets except E-OBS, while E-OBS is insignificantly correlated only with GLEAM 3.8a.

Over NEU, across all the datasets SSM varies (Fig. S2a) from around 0.22 to 0.35 $m^3\,m^{-3}$ exhibiting strong interannual variability. All the datasets show the wettest summers during 2012 and 2017, while the driest occurred in 2006 and 2018. The strong drought event in 2018 is mentioned in many previous studies (Rousi et al., 2023; Bakke et al., 2020). EVT interannual variability (Fig. S2c) is less pronounced compared to SSM. However, when the SSM is drier, the EVT is higher, and vice versa, as expected in energy-limited regimes. Similarly, PET (Fig. S2e) indicated high interannual variability among all the datasets, with atmospheric water demand that was the highest for the dry summers of 2006 and 2018, and also 2021 which was still hot but wetter than the previous ones, allowing higher evapotranspiration (Fig. S2e). The correlation matrices for SSM and PET indicate highly positive correlation values among all the datasets, while weaker correlation are shown for EVT in case of SiTHv2, MERRA2, JRA55 with ERA5, FLUXCOM with GLEAM 3.7b, SiTHv2, MERRA2, and JRA55 (Fig. S2d).

Over EEU, the interannual variability is higher for SSM (Fig. S2g) and EVT (Fig. S2i) compared to PET (Fig. S2k). All the datasets show driest SSM during 2006, 2010, 2018, and 2021, and wettest during 2003, 2008, 2017, 2019, and 2022 (except in JRA55, where few of these are shifted by a year). The high EVT are seen during 2004, 2007, 2011, 2013, 2016, 2022 and low in 2003, 2006, 2010,2012, 2014, 2015, 2017, 2019. All the datasets capture the well known extremely hot and dry summer of 2010 over EEU, that was subject of several previous studies (Barriopedro et al., 2011; Lhotka and Kyselỳ, 2015; Lebedeva et al., 2016). During the summer of 2010, the soil is so dry that there is no moisture left to meet the enormous atmospheric demand of water supply associated with the severe heat hitting the region. For this region, all the datasets are highly positively correlated among each other for all the variables except JRA55 with ERA5land for EVT.

WCE, similar to MED (Fig. 3), shows SSM (Fig. S3a) dips in the summers of 2003 and 2022, known to be characterized by widespread hot and dry conditions (Dosio et al., 2023; Herrera-Lormendez et al., 2023; Rebetez et al., 2006), while the summers of 2004 and 2021 are wet and relatively cool (Fig. S3e). In WCE, the extremely hot and dry summer of 2015 (Orth et al., 2016; Hoy et al., 2017) is also detected by all soil moisture datasets. Conversely, responses are different in terms of the EVT, as shown by the timeseries (Fig. S3c). For example, JRA55 and SiTHv2 show increasing evaporation during low SSM years, while MERRA2 shows peaks in EVT not detected by any other dataset. For EVT, the datasets SiTHv2, FLUXCOM, JRA55 and MERRA2 are weakly correlated with one another and other datasets. PET for WCE (Fig. S3e) interannual variability follows similar pattern for all datasets except JRA55 which is reflected in the correlation matrix (Fig. S3f).

The comparison of the different PET methods for interannual variation (Fig. S4) reveals a wide range of PET variability, with some methods exhibiting inconsistent interannual patterns for the same region and even within the same dataset. Across all the regions, PET derived from the Thornthwaite method consistently exhibits the highest values (except for MED). Only for MED, Penman–Monteith method indicates different pattern than rest of the methods and GLEAM versions. GLEAM (both versions) systematically produces lower PET values across regions (except for NEU).

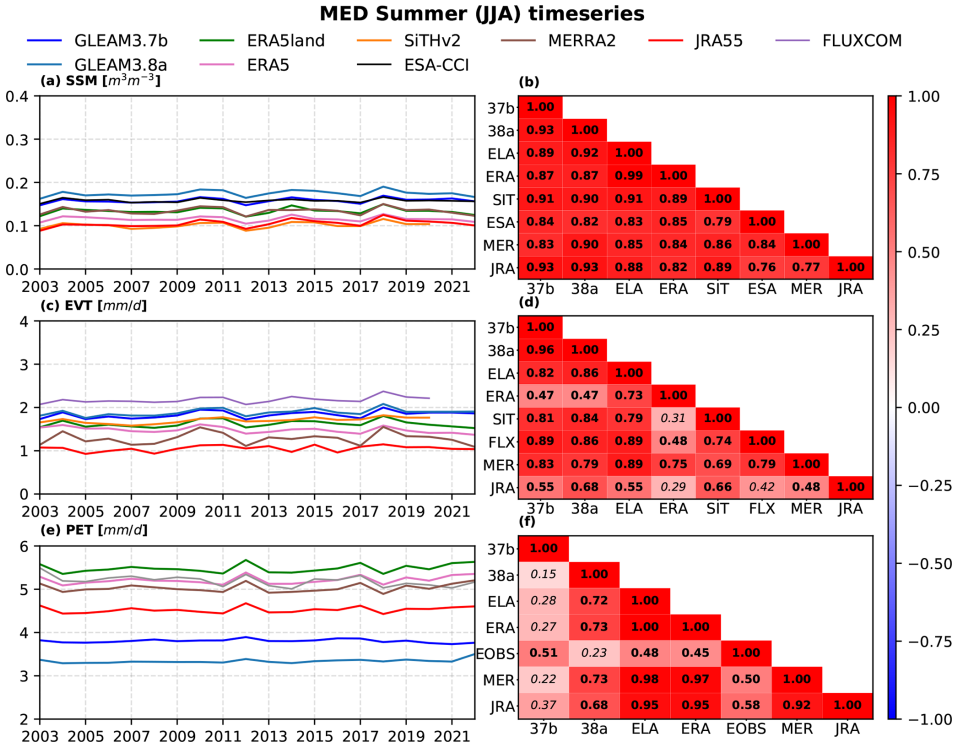


Figure 3. Timeseries (left) and correlation matrices (right) of SSM, EVT, and PET over MED. In the correlation matrices the datasets names are abbreviated as follows: GLEAM 3.7b as 37b, GLEAM 3.8a as 38a, ERA5land as ELA, ERA5 as ERA, ESA-CCI as ESA, SiTHv2 as SIT, FLUXCOM as FLX, MERRA2 as MER, and JRA55 as JRA. The correlation coefficient values in bold are significant at 95 % level and non-significant correlations are in italic.

The correlation matrices (Fig. S5) show strong agreement among datasets for all the regions except for MED, suggesting that interannual PET variability in these regions is relatively insensitive to methodological differences. For MED, the Penman–Monteith method shows negative correlation coefficient with GLEAM both versions, Hargreaves and Baier's methods, while PET from the rest of the methods indicate high positive correlation with GLEAM 3.8a and among themselves.

3.2 Land-atmosphere coupling

We now explore the relationships among these variables to gain deeper insights into the spatial variability patterns of land–atmosphere coupling. Here, we first investigate the scatter plots and linear regression analysis (Figs. 4 and 5) between 2 m mean air temperature (TAS), SSM, EVT.

Previous studies have identified transitional evaporative regimes as hot spots of soil moisture–temperature coupling (Gevaert et al., 2018; Schwitalla et al., 2025). In these regions, evaporation is both sufficiently variable and strongly controlled by soil moisture availability, allowing it to significantly influence atmospheric variability. In contrast, soil moisture is generally not a limiting factor in wetter regions, where evaporation is predominantly driven by radiation. Meanwhile, in drier regions, both soil moisture and evaporation exhibit limited variability, reducing their influence on air temperature dynamics. The SSM and EVT relation represents the terrestrial leg of the coupling. In contrast, EVT and TAS relations explain the atmosphere leg of the coupling, and SSM and TAS relations indicate the combination of both,i.e., land-atmosphere coupling (overall coupling).

In general, during summer, evaporation increases with increasing temperature, and this leads to a reduction in the surface soil moisture. When soil water starts being scarce, plants reduce transpiration. Therefore, despite high radiation and temperature, evapotranspiration decreases and soil moisture too. This, in turn, increases the gap between EVT and PET (the latter is not limited by water), which actually becomes substantial. This will, in turn, lead the boundary layer to warm further due to scarce evaporative cooling, making that particular region prone to longer-lasting and more intense heatwaves (Mueller and Seneviratne, 2012; Materia et al., 2022). This feedback mechanism can be durable and lead to further increases in temperature and finally drought conditions (Miralles et al., 2019).

Over NEU, SSM decreases with increasing TAS during summer across all datasets (Fig. 4a). However, the atmospheric coupling indicates a positive relation (Fig. 4c), sug-

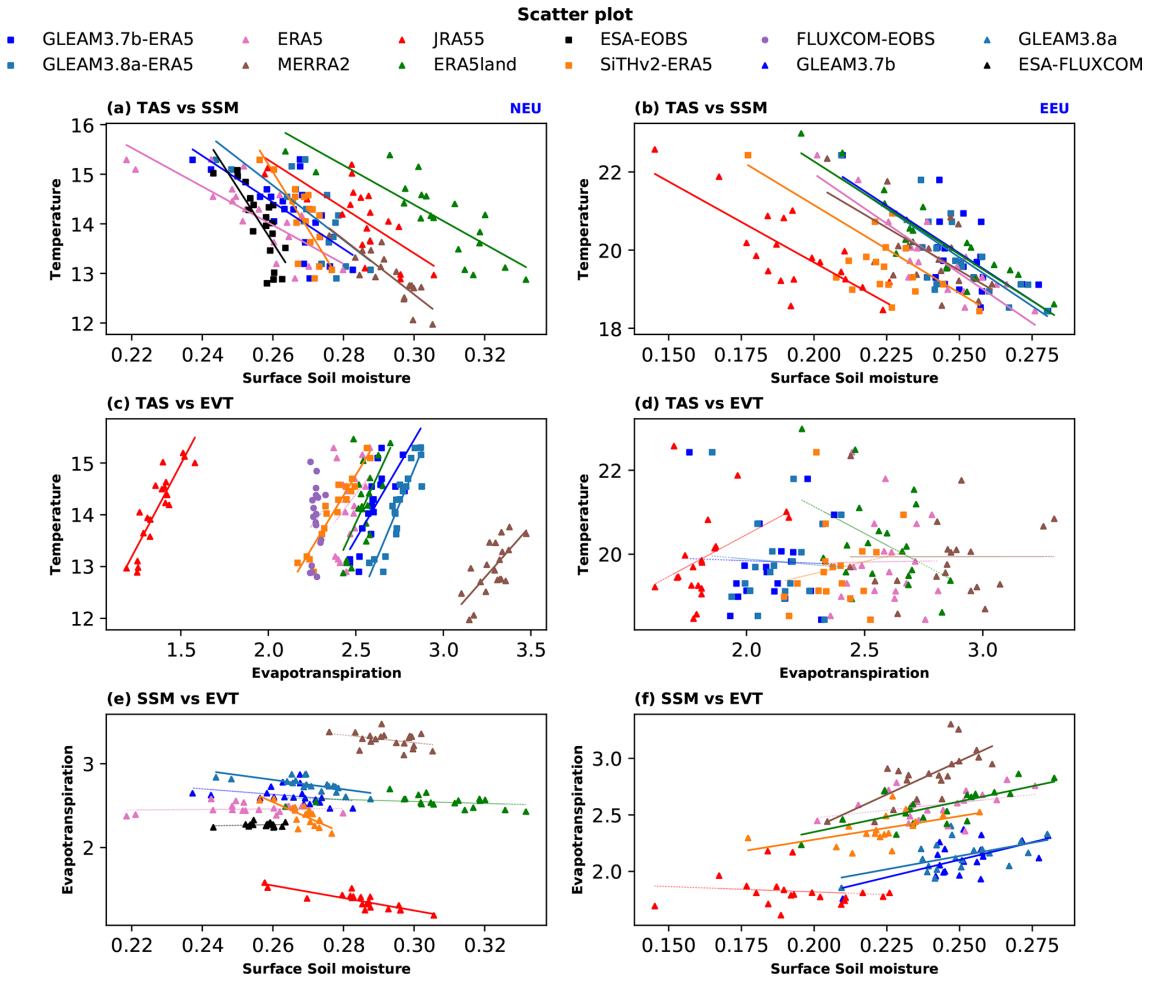


Figure 4. Scatter plot and linear regression (on the left for NEU and on the right for EEU) between SSM, EVT, TAS. The thick line indicates linear regression significance at 95 % level, and the dashed line indicates the regression is not significant.

gesting that EVT is primarily controlled by available energy rather than SSM. The weak dependence of EVT on SSM (Fig. 4e) further supports the characterization of NEU as an energy-limited region during summer, where enhanced solar radiation drives evaporation even under decreasing soil moisture conditions.

For EEU, the coupling between TAS and SSM, as well as the land coupling, shows significant relationships across most datasets (Fig. 4b, f), while the atmospheric coupling remains largely insignificant (Fig. 4d). This indicates that although SSM and TAS are coupled, variations in SSM do not consistently translate into changes in EVT. The lack of a coherent TAS–EVT relationship likely reflects strong spatial heterogeneity among datasets, and the area average of this nullifies both positive and negative relations.

Over WCE, correlations are generally significant across all coupling components. The atmospheric coupling (Fig. 5c) exhibits a steep positive slope, indicating that relatively small changes in EVT are associated with comparatively large TAS responses (except MERRA2 and FLUXCOM) which reflects in the overall coupling (Fig. 5a) with steep negative slopes indicating small changes in SSM lead to a big change in TAS. At the same time, the land coupling (Fig. 5e) shows a decrease in EVT with declining SSM (except SiTHv2 and JRA55 which show negative slopes), identifying WCE as a predominantly water-limited region during summer.

In the MED region, the negative atmospheric coupling (Fig. 5d) indicates a water-limited regime, where EVT is decreasing despite of increasing TAS. The overall and terrestrial coupling (Fig. 5b, f) show patterns similar to WCE but with steeper slopes, pointing to a stronger moisture limitation. Although correlations across coupling components are generally significant, land–atmosphere interactions in MED are primarily governed by SSM availability rather than energy, resulting in suppressed EVT during summer and enhanced near-surface warming.

Using scatter plot and linear regression analysis, we examined the general picture of land and atmosphere coupling dur-

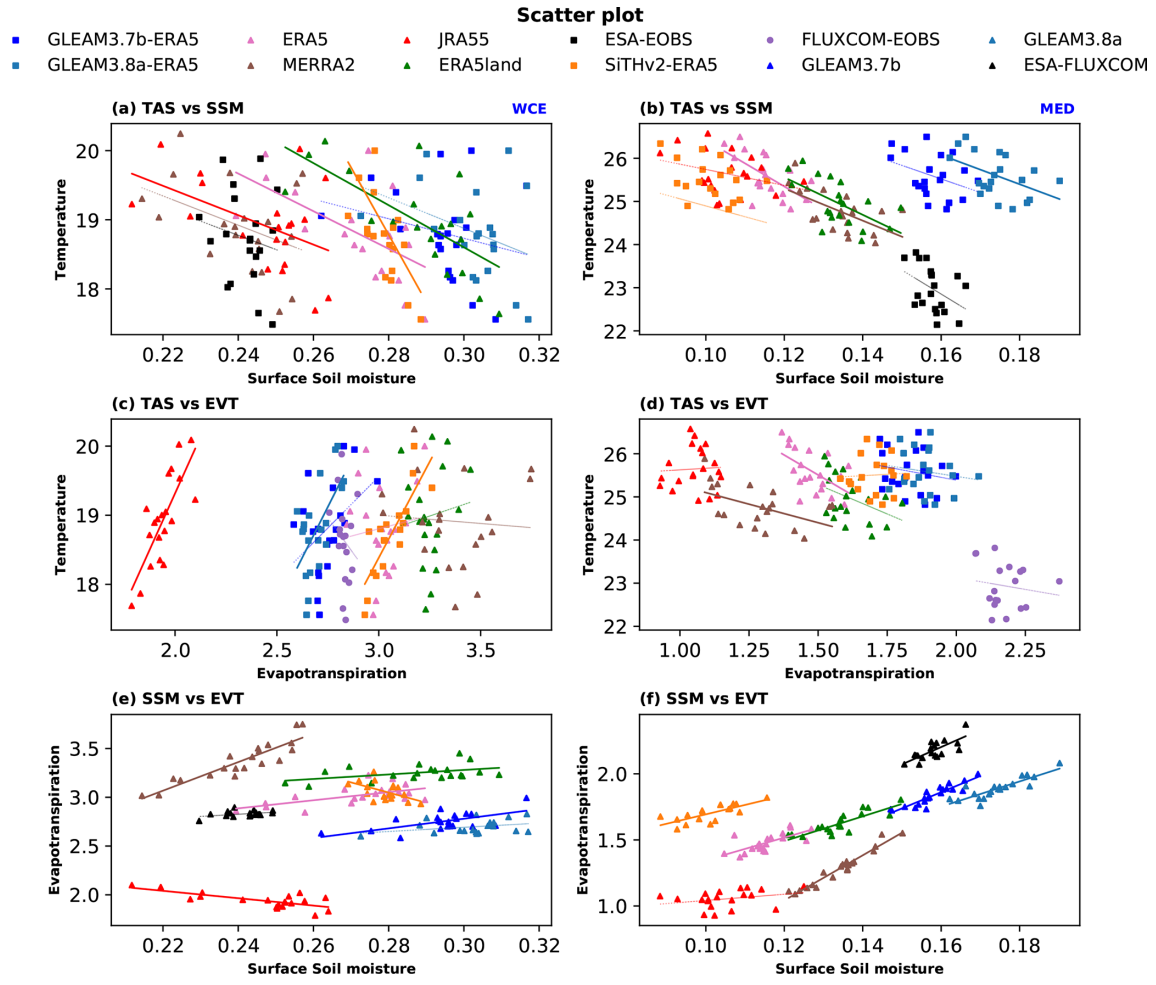


Figure 5. Same as Fig. 4, but for WCE (left), MED (right).

ing summer in the four European IPCC regions. Although the datasets varied in their ranges, they exhibited mostly similar coupling relationship within each region. However, a limitation of this analysis is that it may mask important spatial variations within regions, as strong localized relationships can dominate and skew the area-averaged results, as observed in EEU for the relationship between TAS and EVT. Therefore, a more detailed spatial analysis of land–atmosphere coupling is necessary to capture regional heterogeneity and underlying patterns better, and here we investigated the correlation (Fig. 6) and regression (Fig. 7) among TAS, EVT and SSM over the entire Europe.

The spatial coupling analysis also indicates that, irrespective of actual values of the variables, all the datasets represent similar relationships among the variables, except JRA55, where the land coupling and the atmospheric coupling pattern do not match the rest of the datasets. Overall, the spatial coupling relations over Europe match the regional spatial averaged analysis that we discussed earlier, with Northern Europe being an energy-limited region and the southern part being a water-limited region. For example, if we focus on a water-limited region like Spain, then the atmospheric coupling shows a significant negative relation, indicating that as the temperature rises during summer, the evaporation actually decreases. The land coupling represents that the increase in soil moisture leads to an increase in evapotranspiration. Similarly, over an energy-limited region like Scandinavia, where the pattern is reversed as compared to Spain. Therefore, when we investigate the overall coupling of temperature with soil moisture, it is negative all over Europe, but in northern Europe, the energy is limited, therefore, the increase in temperature leads to enhanced atmospheric demand of water, which is then met by the water supply via evapotranspiration from soil moisture. In contrast, for southern Europe, the soil moisture is the limiting factor during summer, when the temperature is high, but still the low soil moisture can not meet the atmospheric demand for water, which further keeps rising the temperature. Here, we found that the southern part of France has a significant positive relation between

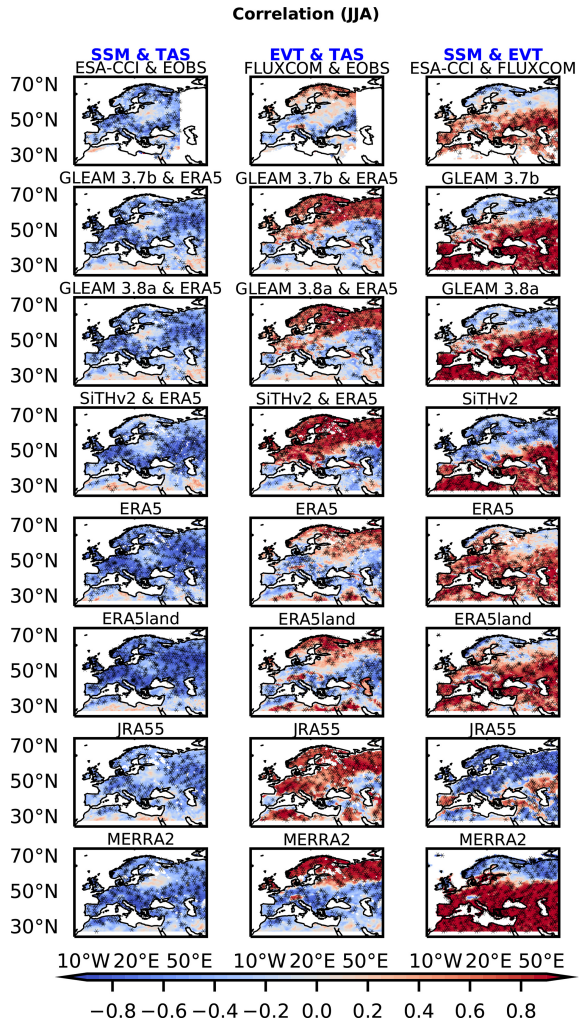


Figure 6. Correlation map of: (left) SSM and TAS, (centre) EVT and TAS, and (right) SSM and EVT. The black dots represent correlation coefficients significant at 95 % level.

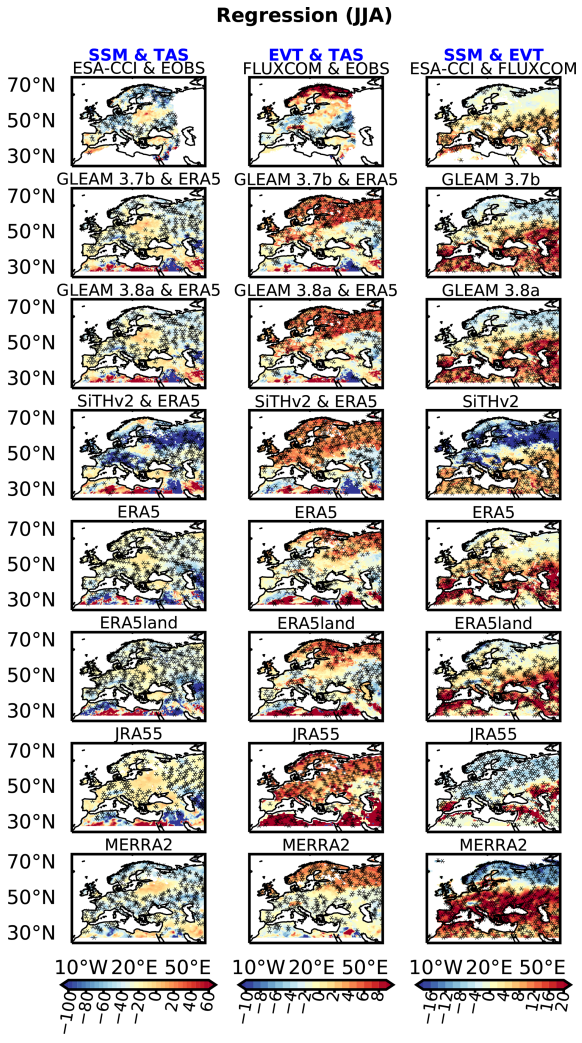


Figure 7. Same as Fig. 6, but showing the slope of the linear regression.

SSM and EVT (land coupling), as well as between EVT and TAS (atmospheric coupling).

4 Discussion and Conclusions

In this study, we examine the similarities and differences among multiple gridded observations-based datasets in capturing the interannual variability of key surface parameters involved in land-atmosphere coupling, such as the surface soil moisture, evapotranspiration, potential evapotranspiration, and 2 m air temperature, across Europe during summer. We further performed an extensive analysis of differences and similarities in the representation of coupling relationships at the land-atmosphere interface, whose impact on heat extremes is well established for regions in transitional evaporative regime.

Despite a wide range of absolute values, the datasets exhibit broadly similar patterns in their summer interannual variability and land-atmospheric coupling relationships. However, regional differences are evident in evapotranspiration and potential evapotranspiration across different datasets, especially in WCE and MED where transitional regimes are dominant. In particular, SiTHv2 and JRA55 exhibit different patterns compared to the other datasets in representing the absolute values of state variables and land–atmosphere coupling. Surface soil moisture exhibits strong agreements across all datasets, showing significant correlations, yet it still displays a wide range of interannual variation and different annual cycles in SiTHv2 and MERRA2.

Analysis of land–atmosphere coupling indicates that northern Europe (energy-limited regime) exhibits stronger atmospheric coupling, while southern Europe (water-limited regime) is dominated by terrestrial coupling; this pattern is well represented across all datasets except JRA55. All

datasets consistently capture the large-scale north–south gradient in coupling strength, with weak coupling in northern Europe, strong coupling in southern Europe, and central Europe where evapotranspiration is alternatively controlled by radiation and soil moisture, switching between a wet regime to a transitional one across different years but also within the same season. This spatial structure is in good agreement with previous studies (Seneviratne et al., 2006; Knist et al., 2017). A similar analysis was performed by Mei and Wang (2012), who examined land–atmosphere coupling strength over the United States. However, these earlier studies primarily focused on evaluating regional model skill relative to observations, whereas the present study goes beyond this by inter-comparing multiple observational datasets themselves, thereby highlighting the role of observational uncertainty in diagnosing land–atmosphere coupling over Europe.

We conclude that large uncertainties persist in the absolute values of the state variables involved in land-atmosphere coupling processes. However, the interannual variability of such variables is consistently represented across most of the different observations-based datasets. Some datasets (e.g., JRA55, MERRA2, SiTHv2) exhibit distinct regional time series patterns with partly unplausible features, reflected also in their spatiotemporal coupling characteristics. In general, the representation of land, atmospheric, and combined coupling is comparable across datasets; however, evapotranspiration in JRA55 stands out as a major source of discrepancy, which leads to a misrepresentation of land and atmospheric coupling separately.

Code availability. The codes underlying the analyses presented in this study are openly available through the Zenodo repository https://doi.org/10.5281/zenodo.24199689 (Sahoo, 2026).

Data availability. All the data are taken from respective open sources and are freely downloadable.

Supplement. The supplement related to this article is available online at https://doi.org/10.5194/hess-30-7301-2026-supplement.

Author contributions. The study was conceptualized and structured by MS, MD, and SM. All figures were generated, and the first draft of the manuscript was written by MS. MD and SM contributed to improving the writing and provided critical feedback throughout the development of the manuscript.

Competing interests. The contact author has declared that none of the authors has any competing interests.

Disclaimer. Publisher's note: Copernicus Publications remains neutral with regard to jurisdictional claims made in the text, published maps, institutional affiliations, or any other geographical representation in this paper. The authors bear the ultimate responsibility for providing appropriate place names. Views expressed in the text are those of the authors and do not necessarily reflect the views of the publisher.

Acknowledgements. The authors are very thankful to the two anonymous reviewers for their constructive comments. We gratefully acknowledge all data providers for making their datasets freely available. We sincerely thank Margarida Samso Cabre for downloading the datasets and resolving related issues, which greatly supported this work. MS acknowledges the HPC support provided by BSC, which enabled the data analysis. MS is also grateful to Alvise Aranyossy and Lina Teckentrup for valuable scientific discussions and assistance with the potential evapotranspiration calculations. Special thanks are extended to Charlotte Bohne and Nuria Perez Zanon for their help in improving the manuscript.

Financial support. This work was supported by the Horizon Europe project CERISE (grant no. 101082139), funded by the European Union. Views and opinions expressed are, however, those of the author(s) only and do not necessarily reflect those of the European Union or the Commission. Neither the European Union nor the granting authority can be held responsible for them.

Review statement. This paper was edited by Adriaan J. (Ryan) Teuling and reviewed by two anonymous referees.

References

Allen, R. G., Pereira, L. S., Smith, M., Raes, D., and Wright, J. L.: Crop evapotranspiration-Guidelines for computing crop water requirements-FAO Irrigation and drainage paper 56, Fao, Rome, 300, D05109, https://doi.org/10.1061/(ASCE)0733-9437(2005)131:1(2), 1998.

Baier, W. and Robertson, G. W.: Estimation of latent evaporation from simple weather observations, Can. J. Plant Sci., 45, 276–284, 1965.

Bakke, S. J., Ionita, M., and Tallaksen, L. M.: The 2018 northern European hydrological drought and its drivers in a historical perspective, Hydrol. Earth Syst. Sci., 24, 5621–5653, https://doi.org/10.5194/hess-24-5621-2020, 2020.

Baldocchi, D. and Meyers, T.: On using eco-physiological, micrometeorological and biogeochemical theory to evaluate carbon dioxide, water vapor and trace gas fluxes over vegetation: a perspective, Agr. Forest Meteorol., 90, 1–25, 1998.

Baret, F., Weiss, M., Lacaze, R., Camacho, F., Makhmara, H., Pacholcyzk, P., and Smets, B.: GEOV1: LAI and FAPAR essential climate variables and FCOVER global time series capitalizing over existing products. Part1: Principles of development and production, Remote Sens. Environ., 137, 299–309, 2013.

Barriopedro, D., Fischer, E. M., Luterbacher, J., Trigo, R. M., and García-Herrera, R.: The hot summer of 2010: redrawing the temperature record map of Europe, Science, 332, 220–224, 2011.

Beck, H. E., Van Dijk, A. I., Larraondo, P. R., McVicar, T. R., Pan, M., Dutra, E., and Miralles, D. G.: MSWX: global 3-hourly 0.1 bias-corrected meteorological data including near-real-time updates and forecast ensembles, B. Am. Meteorol. Soc., 103, E710–E732, 2022.

Beillouin, D., Schauberger, B., Bastos, A., Ciais, P., and Makowski, D.: Impact of extreme weather conditions on European crop production in 2018, Philos. T. Roy. Soc. B, 375, 20190510, https://doi.org/10.1098/rstb.2019.0510, 2020.

Byrne, M. P.: Amplified warming of extreme temperatures over tropical land, Nat. Geosci., 14, 837–841, 2021.

Cook, B. I., Smerdon, J. E., Seager, R., and Coats, S.: Global warming and 21 st century drying, Clim. Dynam., 43, 2607–2627, 2014.

Cornes, R. C., van der Schrier, G., van den Besselaar, E. J., and Jones, P. D.: An ensemble version of the E-OBS temperature and precipitation data sets, J. Geophys. Res.-Atmos., 123, 9391–9409, 2018.

Dee, D. P., Uppala, S., Simmons, A. J., Berrisford, P., Poli, P., Kobayashi, S., Andrae, U., Balmaseda, M. A., Balsamo, G., Bauer, D. P., and Bechtold, P.: The ERA-Interim reanalysis: Configuration and performance of the data assimilation system, Q. J. Roy. Meteor. Soc., 137, 553–597, 2011.

Dembélé, M., Ceperley, N., Zwart, S. J., Salvadore, E., Mariethoz, G., and Schaefli, B.: Potential of satellite and reanalysis evaporation datasets for hydrological modelling under various model calibration strategies, Adv. Water Resour., 143, 103667, https://doi.org/10.1016/j.advwatres.2020.103667, 2020.

Denissen, J. M., Teuling, A. J., Pitman, A. J., Koirala, S., Migliavacca, M., Li, W., Reichstein, M., Winkler, A. J., Zhan, C., and Orth, R.: Widespread shift from ecosystem energy to water limitation with climate change, Nat. Clim. Change, 12, 677–684, 2022.

Dirmeyer, P. A.: The hydrologic feedback pathway for land–climate coupling, J. Hydrometeorol., 7, 857–867, 2006.

Dirmeyer, P. A. and Halder, S.: Application of the land–atmosphere coupling paradigm to the operational Coupled Forecast System, version 2 (CFSv2), J. Hydrometeorol., 18, 85–108, 2017.

Dirmeyer, P. A., Wang, Z., Mbuh, M. J., and Norton, H. E.: Intensified land surface control on boundary layer growth in a changing climate, Geophys. Res. Lett., 41, 1290–1294, 2014.

Dirmeyer, P. A., Balsamo, G., Blyth, E. M., Morrison, R., and Cooper, H. M.: Land-atmosphere interactions exacerbated the drought and heatwave over northern Europe during summer 2018, AGU Advances, 2, e2020AV000283, https://doi.org/10.1029/2020AV000283, 2021.

Donat, M. G., Pitman, A. J., and Seneviratne, S. I.: Regional warming of hot extremes accelerated by surface energy fluxes, Geophys. Res. Lett., 44, 7011–7019, 2017.

Donat, M. G., Pitman, A. J., and Angélil, O.: Understanding and reducing future uncertainty in midlatitude daily heat extremes via land surface feedback constraints, Geophys. Res. Lett., 45, 10–627, 2018.

Dorigo, W., Wagner, W., Albergel, C., Albrecht, F., Balsamo, G., Brocca, L., Chung, D., Ertl, M., Forkel, M., Gruber, A., and Haas, E.: ESA CCI Soil Moisture for improved Earth system understanding: State-of-the art and future directions, Remote Sens. Environ., 203, 185–215, 2017.

Dosio, A., Spinoni, J., and Migliavacca, M.: Record-breaking and unprecedented compound hot and dry summers in Europe under different emission scenarios, Environ. Res., 2, 045009, https://doi.org/10.1088/2752-5295/acfa1b, 2023.

Ferguson, C. R., Wood, E. F., and Vinukollu, R. K.: A global intercomparison of modeled and observed land–atmosphere coupling, J. Hydrometeorol., 13, 749–784, 2012.

Fischer, E. M., Seneviratne, S. I., Lüthi, D., and Schär, C.: Contribution of land-atmosphere coupling to recent European summer heat waves, Geophys. Res. Lett., 34, https://doi.org/10.1029/2006GL029068, 2007.

Gelaro, R., McCarty, W., Suárez, M. J., Todling, R., Molod, A., Takacs, L., Randles, C. A., Darmenov, A., Bosilovich, M. G., Reichle, R., and Wargan, K.: The modern-era retrospective analysis for research and applications, version 2 (MERRA-2), J. Climate, 30, 5419–5454, 2017.

Gevaert, A., Miralles, D. G., de Jeu, R. A., Schellekens, J., and Dolman, A. J.: Soil moisture-temperature coupling in a set of land surface models, J. Geophys. Res.-Atmos., 123, 1481–1498, 2018.

Gruber, A., Scanlon, T., van der Schalie, R., Wagner, W., and Dorigo, W.: Evolution of the ESA CCI Soil Moisture climate data records and their underlying merging methodology, Earth Syst. Sci. Data, 11, 717–739, https://doi.org/10.5194/essd-11-717-2019, 2019.

Hargreaves, G. H. and Samani, Z. A.: Estimating potential evapotranspiration, J. Irr. Drain. Div., 108, 225–230, 1982.

Herrera-Lormendez, P., Douville, H., and Matschullat, J.: European summer synoptic circulations and their observed 2022 and projected influence on hot extremes and dry spells, Geophys. Res. Lett., 50, e2023GL104580, https://doi.org/10.1029/2023GL104580, 2023.

Hersbach, H., Bell, B., Berrisford, P., Hirahara, S., Horányi, A., Muñoz-Sabater, J., Nicolas, J., Peubey, C., Radu, R., Schepers, D., and Simmons, A.: The ERA5 global reanalysis, Q. J. Roy. Meteor. Soc., 146, 1999–2049, 2020.

Hirsch, A., Pitman, A., Seneviratne, S. I., Evans, J., and Haverd, V.: Summertime maximum and minimum temperature coupling asymmetry over Australia determined using WRF, Geophys. Res. Lett., 41, 1546–1552, 2014.

Hirschi, M., Seneviratne, S. I., Alexandrov, V., Boberg, F., Boroneant, C., Christensen, O. B., Formayer, H., Orlowsky, B., and Stepanek, P.: Observational evidence for soil-moisture impact on hot extremes in southeastern Europe, Nat. Geosci., 4, 17–21, 2011.

Hoy, A., Hänsel, S., Skalak, P., Ustrnul, Z., and Bochníček, O.: The extreme European summer of 2015 in a long-term perspective, Int. J. Climatol., 37, 943–962, 2017.

Iturbide, M., Gutiérrez, J. M., Alves, L. M., Bedia, J., Cerezo-Mota, R., Cimadevilla, E., Cofiño, A. S., Di Luca, A., Faria, S. H., Gorodetskaya, I. V., Hauser, M., Herrera, S., Hennessy, K., Hewitt, H. T., Jones, R. G., Krakovska, S., Manzanas, R., Martínez-Castro, D., Narisma, G. T., Nurhati, I. S., Pinto, I., Seneviratne, S. I., van den Hurk, B., and Vera, C. S.: An update of IPCC climate reference regions for subcontinental analysis of climate model data: definition and aggregated datasets, Earth Syst.

Sci. Data, 12, 2959–2970, https://doi.org/10.5194/essd-12-2959-2020, 2020.

Jung, M., Koirala, S., Weber, U., Ichii, K., Gans, F., Camps-Valls, G., Papale, D., Schwalm, C., Tramontana, G., and Reichstein, M.: The FLUXCOM ensemble of global land-atmosphere energy fluxes, Scientific Data, 6, 74, https://doi.org/10.1038/s41597-019-0076-8, 2019.

Kew, S. F., Philip, S. Y., Van Oldenborgh, G. J., van der Schrier, G., Otto, F. E., and Vautard, R.: The exceptional summer heat wave in southern Europe 2017, B. Am. Meteorol. Soc., 100, S49–S53, 2019.

Kim, H., Parinussa, R., Konings, A. G., Wagner, W., Cosh, M. H., Lakshmi, V., Zohaib, M., and Choi, M.: Global-scale assessment and combination of SMAP with ASCAT (active) and AMSR2 (passive) soil moisture products, Remote Sens. Environ., 204, 260–275, 2018.

Klein Tank, A. M. G., Wijngaard, J. B., Können, G. P., Böhm, R., Demarée, G., Gocheva, A., Mileta, M., Pashiardis, S., Hejkrlik, L., Kern-Hansen, C., Heino, R., Bessemoulin, P., Müller-Westermeier, G., Tzanakou, M., Szalai, S., Pálsdóttir, T., Fitzgerald, D., Rubin, S., Capaldo, M., Maugeri, M., Leitass, A., Bukantis, A., Aberfeld, R., van Engelen, A. F. V., Forland, E., Mietus, M., Coelho, F., Mares, C., Razuvaev, V., Nieplova, E., Cegnar, T., Antonio López, J., Dahlström, B., Moberg, A., Kirchhofer, W., Ceylan, A., Pachaliuk, O., Alexander, L. V., and Petrovic, P.: Daily dataset of 20th-century surface air temperature and precipitation series for the European Climate Assessment, Int. J. Climatol., 22, 1441–1453, 2002.

Knist, S., Goergen, K., Buonomo, E., Christensen, O. B., Colette, A., Cardoso, R. M., Fealy, R., Fernández, J., García-Díez, M., Jacob, D., and Kartsios, S.: Land-atmosphere coupling in EURO-CORDEX evaluation experiments, J. Geophys. Res.-Atmos., 122, 79–103, 2017.

Kobayashi, S., Ota, Y., Harada, Y., Ebita, A., Moriya, M., Onoda, H., Onogi, K., Kamahori, H., Kobayashi, C., Endo, H., and Miyaoka, K.: The JRA-55 reanalysis: General specifications and basic characteristics, J. Meteorol. Soc. Jpn. Ser. II, 93, 5–48, 2015.

Koster, R. D., Sud, Y. C., Guo, Z., Dirmeyer, P. A., Bonan, G., Oleson, K. W., Chan, E., Verseghy, D., Cox, P., Davies, H., and Kowalczyk, E.: GLACE: the global land–atmosphere coupling experiment. Part I: overview, J. Hydrometeorol., 7, 590–610, 2006.

Lebedeva, M. G., Krymskaya, O. V., Lupo, A. R., Chendev, Y. G., Petin, A. N., and Solovyov, A. B.: Trends in summer season climate for Eastern Europe and Southern Russia in the early 21st century, Adv. Meteorol., 2016, 5035086, https://doi.org/10.1155/2016/5035086, 2016.

Lhotka, O. and Kyselỳ, J.: Hot Central-European summer of 2013 in a long-term context, Int. J. Climatol., 35, https://doi.org/10.1002/joc.4277, 2015.

Li, M., Wu, P., and Ma, Z.: A comprehensive evaluation of soil moisture and soil temperature from third-generation atmospheric and land reanalysis data sets, Int. J. Climatol, 40, 5744–5766, 2020.

Li, W., Migliavacca, M., Forkel, M., Walther, S., Reichstein, M., and Orth, R.: Revisiting global vegetation controls using multi-layer soil moisture, Geophys. Res. Lett., 48, e2021GL092856, https://doi.org/10.1029/2021GL092856, 2021.

Li, W., Migliavacca, M., Forkel, M., Denissen, J. M., Reichstein, M., Yang, H., Duveiller, G., Weber, U., and Orth, R.: Widespread increasing vegetation sensitivity to soil moisture, Nat. Commun., 13, 3959, https://doi.org/10.1038/s41467-022-31667-9, 2022a.

Li, Y., Qin, Y., and Rong, P.: Evolution of potential evapotranspiration and its sensitivity to climate change based on the Thornthwaite, Hargreaves, and Penman–Monteith equation in environmental sensitive areas of China, Atmos. Res., 273, 106178, https://doi.org/10.1016/j.atmosres.2022.106178, 2022b.

Liang, S., Cheng, J., Jia, K., Jiang, B., Liu, Q., Xiao, Z., Yao, Y., Yuan, W., Zhang, X., Zhao, X., and Zhou, J.: The global land surface satellite (GLASS) product suite, B. Am. Meteorol. Soc., 102, E323–E337, 2021.

Logan, T., Aoun, A., Bourgault, P., Dupuis, É., Huard, D., Lavoie, J., Rondeau-Genesse, G., Smith, T. J., Alegre, R., Barnes, C., and Biner, S.: Ouranosinc/xclim: v0. 39.0, Zenodo [code], https://doi.org/10.5281/zenodo.7274811, 2022.

Lorenz, R., Jaeger, E. B., and Seneviratne, S. I.: Persistence of heat waves and its link to soil moisture memory, Geophys. Res. Lett., 37, https://doi.org/10.1029/2010GL042764, 2010.

Martens, B., Miralles, D. G., Lievens, H., van der Schalie, R., de Jeu, R. A. M., Fernández-Prieto, D., Beck, H. E., Dorigo, W. A., and Verhoest, N. E. C.: GLEAM v3: satellite-based land evaporation and root-zone soil moisture, Geosci. Model Dev., 10, 1903–1925, https://doi.org/10.5194/gmd-10-1903-2017, 2017.

Materia, S., Ardilouze, C., Prodhomme, C., Donat, M. G., Benassi, M., Doblas-Reyes, F. J., Peano, D., Caron, L.-P., Ruggieri, P., and Gualdi, S.: Summer temperature response to extreme soil water conditions in the Mediterranean transitional climate regime, Clim. Dynam., 58, 1943–1963, 2022.

Mei, R. and Wang, G.: Summer land–atmosphere coupling strength in the United States: Comparison among observations, reanalysis data, and numerical models, J. Hydrometeorol., 13, 1010–1022, 2012.

Miralles, D. G., Holmes, T. R. H., De Jeu, R. A. M., Gash, J. H., Meesters, A. G. C. A., and Dolman, A. J.: Global land-surface evaporation estimated from satellite-based observations, Hydrol. Earth Syst. Sci., 15, 453–469, https://doi.org/10.5194/hess-15-453-2011, 2011.

Miralles, D. G., Teuling, A. J., Van Heerwaarden, C. C., and Vilà-Guerau de Arellano, J.: Mega-heatwave temperatures due to combined soil desiccation and atmospheric heat accumulation, Nat. Geosci., 7, 345–349, 2014.

Miralles, D. G., Gentine, P., Seneviratne, S. I., and Teuling, A. J.: Land–atmospheric feedbacks during droughts and heatwaves: state of the science and current challenges, Ann. NY Acad. Sci., 1436, 19–35, 2019.

Moratiel, R., Bravo, R., Saa, A., Tarquis, A. M., and Almorox, J.: Estimation of evapotranspiration by the Food and Agricultural Organization of the United Nations (FAO) Penman–Monteith temperature (PMT) and Hargreaves–Samani (HS) models under temporal and spatial criteria – a case study in Duero basin (Spain), Nat. Hazards Earth Syst. Sci., 20, 859–875, https://doi.org/10.5194/nhess-20-859-2020, 2020.

Mousa, B. and Shu, H.: Spatial evaluation and assimilation of SMAP, SMOS, and ASCAT satellite soil moisture products over Africa using statistical techniques, Astr. Soc. P., 7, e2019EA000841, https://doi.org/10.1029/2019EA000841, 2020.

Mueller, B. and Seneviratne, S. I.: Hot days induced by precipitation deficits at the global scale, P. Natl. Acad. Sci. USA, 109, 12398–12403, 2012.

Mukherjee, S., Mishra, A. K., Zscheischler, J., and Entekhabi, D.: Interaction between dry and hot extremes at a global scale using a cascade modeling framework, Nat. Commun., 14, 277, https://doi.org/10.1038/s41467-022-35748-7, 2023.

Muñoz-Sabater, J., Dutra, E., Agustí-Panareda, A., Albergel, C., Arduini, G., Balsamo, G., Boussetta, S., Choulga, M., Harrigan, S., Hersbach, H., Martens, B., Miralles, D. G., Piles, M., Rodríguez-Fernández, N. J., Zsoter, E., Buontempo, C., and Thépaut, J.-N.: ERA5-Land: a state-of-the-art global reanalysis dataset for land applications, Earth Syst. Sci. Data, 13, 4349–4383, https://doi.org/10.5194/essd-13-4349-2021, 2021.

Nguyen, H. H., Kim, H., and Choi, M.: Evaluation of the soil water content using cosmic-ray neutron probe in a heterogeneous monsoon climate-dominated region, Adv. Water Resour., 108, 125–138, 2017.

Orth, R., Zscheischler, J., and Seneviratne, S. I.: Record dry summer in 2015 challenges precipitation projections in Central Europe, Sci. Rep., 6, 28334, https://doi.org/10.1038/srep28334, 2016.

Philip, S. Y., Kew, S. F., Hauser, M., Guillod, B. P., Teuling, A. J., Whan, K., Uhe, P., and Oldenborgh, G. J. v.: Western US high June 2015 temperatures and their relation to global warming and soil moisture, Clim. Dynam., 50, 2587–2601, 2018.

Preimesberger, W., Scanlon, T., Su, C.-H., Gruber, A., and Dorigo, W.: Homogenization of structural breaks in the global ESA CCI soil moisture multisatellite climate data record, IEEE T. Geosci. Remote, 59, 2845–2862, 2020.

Preimesberger, W., Stradiotti, P., and Dorigo, W.: ESA CCI Soil Moisture GAPFILLED: an independent global gap-free satellite climate data record with uncertainty estimates, Earth Syst. Sci. Data, 17, 4305–4329, https://doi.org/10.5194/essd-17-4305-2025, 2025.

Priestley, C. H. B. and Taylor, R. J.: On the assessment of surface heat flux and evaporation using large-scale parameters, Mon. Weather Rev., 100, 81–92, 1972.

Quesada, B., Vautard, R., Yiou, P., Hirschi, M., and Seneviratne, S. I.: Asymmetric European summer heat predictability from wet and dry southern winters and springs, Nat. Clim. Change, 2, 736–741, 2012.

Ratna, S. B., Ratnam, J., Behera, S. K., Cherchi, A., Wang, W., and Yamagata, T.: The unusual wet summer (July) of 2014 in Southern Europe, Atmos. Res., 189, 61–68, 2017.

Rebetez, M., Mayer, H., Dupont, O., Schindler, D., Gartner, K., Kropp, J. P., and Menzel, A.: Heat and drought 2003 in Europe: a climate synthesis, Ann. Forest Sci., 63, 569–577, 2006.

Rousi, E., Fink, A. H., Andersen, L. S., Becker, F. N., Beobide-Arsuaga, G., Breil, M., Cozzi, G., Heinke, J., Jach, L., Niermann, D., Petrovic, D., Richling, A., Riebold, J., Steidl, S., Suarez-Gutierrez, L., Tradowsky, J. S., Coumou, D., Düsterhus, A., Ellsäßer, F., Fragkoulidis, G., Gliksman, D., Handorf, D., Haustein, K., Kornhuber, K., Kunstmann, H., Pinto, J. G., Warrach-Sagi, K., and Xoplaki, E.: The extremely hot and dry 2018 summer in central and northern Europe from a multi-faceted weather and climate perspective, Nat. Hazards Earth Syst. Sci., 23, 1699–1718, https://doi.org/10.5194/nhess-23-1699-2023, 2023.

Sahoo, M.: Summer Land-Atmosphere Coupling over Europe: A Comparative Evaluation of Observation-based Datasets, Zenodo [code], https://doi.org/10.5281/zenodo.24199689, 2026.

Santanello Jr., J. A., Peters-Lidard, C. D., and Kumar, S. V.: Diagnosing the sensitivity of local land–atmosphere coupling via the soil moisture–boundary layer interaction, J. Hydrometeorol., 12, 766–786, 2011.

Schlesinger, W. H. and Jasechko, S.: Transpiration in the global water cycle, Agr. Forest Meteorol., 189, 115–117, 2014.

Schwitalla, T., Jach, L., Wulfmeyer, V., and Warrach-Sagi, K.: Soil moisture–atmosphere coupling strength over central Europe in the recent warming climate, Nat. Hazards Earth Syst. Sci., 25, 1405–1424, https://doi.org/10.5194/nhess-25-1405-2025, 2025.

Seneviratne, S. I., Lüthi, D., Litschi, M., and Schär, C.: Land–atmosphere coupling and climate change in Europe, Nature, 443, 205–209, 2006.

Seneviratne, S. I., Corti, T., Davin, E. L., Hirschi, M., Jaeger, E. B., Lehner, I., Orlowsky, B., and Teuling, A. J.: Investigating soil moisture–climate interactions in a changing climate: A review, Earth-Sci. Rev., 99, 125–161, 2010.

Seo, Y.-W. and Ha, K.-J.: Changes in land-atmosphere coupling increase compound drought and heatwaves over northern East Asia, Npj Climate and Atmospheric Science, 5, 100, https://doi.org/10.1038/s41612-022-00325-8, 2022.

Sherwood, S. and Fu, Q.: A drier future?, Science, 343, 737–739, 2014.

Thorne, P. and Vose, R.: Reanalyses suitable for characterizing long-term trends, B. Am. Meteorol. Soc., 91, 353–362, 2010.

Thornthwaite, C. W.: An approach toward a rational classification of climate, Geogr. Rev., 38, 55–94, 1948.

Trajkovic, S.: Hargreaves versus Penman-Monteith under humid conditions, J. Irr. Drain. E., 133, 38–42, 2007.

Tran, B. N., van der Kwast, J., Seyoum, S., Uijlenhoet, R., Jewitt, G., and Mul, M.: Uncertainty assessment of satellite remote-sensing-based evapotranspiration estimates: a systematic review of methods and gaps, Hydrol. Earth Syst. Sci., 27, 4505–4528, https://doi.org/10.5194/hess-27-4505-2023, 2023.

Trenberth, K. E., Fasullo, J. T., and Kiehl, J.: Earth's global energy budget, B. Am. Meteorol. Soci., 90, 311–324, 2009.

Vautard, R., Yiou, P., D'andrea, F., De Noblet, N., Viovy, N., Cassou, C., Polcher, J., Ciais, P., Kageyama, M., and Fan, Y.: Summertime European heat and drought waves induced by wintertime Mediterranean rainfall deficit, Geophys. Res. Lett., 34, https://doi.org/10.1029/2006GL028001, 2007.

Wieder, W., Boehnert, J., Bonan, G., and Langseth, M.: Regridded harmonized world soil database v1.2, ORNL Distributed Active Archive Center [data set], https://doi.org/10.3334/ORNLDAAC/1247, 2014.

Wilcox, L. J., Yiou, P., Hauser, M., Lott, F. C., van Oldenborgh, G. J., Colfescu, I., Dong, B., Hegerl, G., Shaffrey, L., and Sutton, R.: Multiple perspectives on the attribution of the extreme European summer of 2012 to climate change, Clim. Dynam., 50, 3537–3555, 2018.

Williams, I. N. and Torn, M. S.: Vegetation controls on surface heat flux partitioning, and land-atmosphere coupling, Geophys. Res. Lett., 42, 9416–9424, 2015.

Winkler, K., Fuchs, R., Rounsevell, M., and Herold, M.: Global land use changes are four times greater than previously esti-

mated, Nat. Commun., 12, 2501, https://doi.org/10.1038/s41467-021-22702-2, 2021.

Wu, Z., Feng, H., He, H., Zhou, J., and Zhang, Y.: Evaluation of soil moisture climatology and anomaly components derived from ERA5-land and GLDAS-2.1 in China, Water Resour. Manag., 35, 629–643, 2021.

Xu, C., Wang, W., Hu, Y., and Liu, Y.: Evaluation of ERA5, ERA5-Land, GLDAS-2.1, and GLEAM potential evapotranspiration data over mainland China, Journal of Hydrology: Regional Studies, 51, 101651, https://doi.org/10.1016/j.ejrh.2023.101651, 2024.

Yi, K., Senay, G. B., Fisher, J. B., Wang, L., Suvočarev, K., Chu, H., Moore, G. W., Novick, K. A., Barnes, M. L., Keenan, T. F., and Mallick, K.: Challenges and future directions in quantifying terrestrial evapotranspiration, Water Resour. Res., 60, e2024WR037622, https://doi.org/10.1029/2024WR037622, 2024.

Zhang, K., Chen, H., Ma, N., Shang, S., Wang, Y., Xu, Q., and Zhu, G.: A global dataset of terrestrial evapotranspiration and soil moisture dynamics from 1982 to 2020, Scientific Data, 11, 445, https://doi.org/10.1038/s41597-024-03271-7, 2024.

Zheng, C., Jia, L., and Zhao, T.: A 21-year dataset (2000–2020) of gap-free global daily surface soil moisture at 1-km grid resolution, Scientific Data, 10, 139, https://doi.org/10.1038/s41597-023-01991-w, 2023.

Zhuo, L., Han, D., Dai, Q., Islam, T., and Srivastava, P. K.: Appraisal of NLDAS-2 multi-model simulated soil moistures for hydrological modelling, Water Resour. Manag., 29, 3503–3517, 2015.